Journal of Quantitative Spectroscopy & Radiative Transfer 110 (2009) 687–699

Contents lists available at ScienceDirect

Journal of Quantitative Spectroscopy & Radiative Transfer

journal homepage: www.elsevier.com/locate/jqsrt

Theoretical calculations of N_2-broadened half-widths of v_5 transitions of HNO_3

A. Laraia [a], R.R. Gamache [a,*], J.-M. Hartmann [b], A. Perrin [b], L. Gomez [b]

[a] University of Massachusetts Lowell and University of Massachusetts School of Marine Sciences, Department of Environmental, Earth, and Atmospheric Sciences, 265 Riverside Street, Lowell, MA 01854-5045, USA

[b] Laboratoire Interuniversitaire des Systèmes Atmosphériques (LISA, CNRS UMR 7584) CNRS and Universities Paris 12 and Paris 7, 61 Av. Général de Gaulle, 94010 Créteil Cedex, France

ARTICLE INFO

Article history:
Received 6 November 2008
Received in revised form
3 February 2009
Accepted 5 February 2009

Keywords:
Complex Robert Bonamy formalism
Half-width
HNO_3
N_2-broadening
Temperature dependence of half-width
Vibrational and rotational state dependence

ABSTRACT

A number of satellite instruments are measuring nitric acid, HNO_3, in the Earth's atmosphere. In order to do retrievals of temperature and concentration profiles, the spectral parameters for many thousands of HNO_3 transitions must be known. Currently the HITRAN database uses a constant estimated value for the air-broadened half-width of HNO_3. To help improve the line shape parameters, complex Robert–Bonamy calculations were made to determine N_2-broadened half-widths for some 5000 transitions of HNO_3 in the v_5 band. The intermolecular potential is a sum of electrostatic terms (dipole–quadrupole and quadrupole–quadrupole) and the atom–atom potential expanded to eighth order. The trajectory parameters were adjusted to yield better agreement with measurement. Velocity integrated calculations were made at seven temperatures in order to determine the temperature dependence of the half-widths. The half-width data are compared with available rotation band measurements. The average percent difference between the measured and calculated half-widths is −2.38 for N_2-broadening and −0.65 for air-broadening. The temperature, vibrational, and rotational state dependence of the half-width are investigated.

1. Introduction

Nitric acid, HNO_3, is an important minor constituent in the Earth's atmosphere. It is the main stratospheric reservoir species of the NO_X family. Photolysis of gas phase HNO_3 releases NO_2, enabling a major pathway for the deactivation of chlorine via the reformation of $ClONO_2$ from NO_2 and ClO. The Polar Stratospheric Clouds (PSCs) that form in the very low temperatures of polar winter remove HNO_3, a key component of PSCs, from the gas phase. PSC particles provide surfaces on which heterogeneous chemical reactions occur that convert chlorine from its reservoir species (e.g., $ClONO_2$, HCl) to the highly reactive forms (e.g., ClO) that participate in the catalytic cycles of ozone destruction. If PSC particles grow large enough they can settle out of the lower stratosphere carrying the HNO_3 with them in a process known as denitrification. When denitrification is severe the formation of $ClONO_2$ is limited, allowing enhanced ClO and thus chemical ozone destruction to persist. Thus HNO_3 has a major role in both the activation and the deactivation of chlorine and indirectly affects the extent, duration, and cumulative magnitude of stratospheric ozone depletion [1–3].

* Corresponding author. Tel.: +1 978 934 3904; fax: +1 978 934 3069.
E-mail address: Robert_Gamache@uml.edu (R.R. Gamache).

0022-4073/$ - see front matter © 2009 Elsevier Ltd. All rights reserved.
doi:10.1016/j.jqsrt.2009.02.003

As a result of the importance of nitric acid's role in the major catalytic cycles for stratospheric ozone loss [4,5] a number of balloon, aircraft, and satellite instruments are retrieving the concentration profiles of HNO_3. In the Polar Aura Validation Experiment (PAVE) Coffey et al. [6] flew the NCAR FTS onboard a NASA DC-8 aircraft to measure a number of constituents, including HNO_3 in the 867.50–871.80 cm^{-1} region, and make comparisons with measurements from the Microwave Limb Sounder (MLS) [7], High Resolution Dynamics Limb Sounder (HIRDLS) [8] and Tropospheric Emission Spectrometer (TES) [9] experiments aboard the Aura satellite. Kinnison et al. [10] report on global observations of HNO_3 made using channels 7, 8, and 9 of the HIRDLS instrument. Santee et al. [11], in a validation of the AURA MLD HNO_3 measurements, compare the data from the MLS 190 and 240 GHz radiometers with data from the balloon measurements; JPL MkIV solar occultation Fourier Transform Infrared (FTIR) spectrometer [12], the Smithsonian Astrophysical Observatory (SAO) far-infrared spectrometer (FIRS-2) [13], and the JPL Submillimeterwave Limb Sounder–2 (SLS-2) [14], with data from aircraft; PAVE, the University of New Hampshire (UNH) Soluble Acidic Gases and Aerosols (SAGA) instrument [15], with the NOAA chemical ionization mass spectrometer (CIMS) [16], and other satellite measurements. The Michelson Interferometer for Passive Atmospheric Sounding (MIPAS) on the European Space Agency (ESA) Environmental Satellite (Envisat) is a high-resolution infrared limb-sounding Fourier-transform spectrometer, which is measuring HNO_3 in the spectral region near 870 cm^{-1} [17,18]. The Swedish-led Odin satellite has the Submillimetre Radiometer (SMR) which observes limb thermal emission from HNO_3 on roughly two measurement days per week using an autocorrelator spectrometer centered at 544.6 GHz [19]. The Improved Limb Atmospheric Spectrometer (ILAS) on board the Advanced Earth Observing Satellite (ADEOS) measured nitric acid profiles from November 1996 to June 1997 at high latitudes in both hemispheres [20]. The Atmospheric Chemistry Experiment Fourier Transform Spectrometer (ACE-FTS) on the Canadian Space Agency's SCISAT-1 mission measures high spectral resolution (0.02 cm^{-1}) solar occultation spectra over the range 750–4400 cm^{-1} [21]. The HNO_3 retrieval is based primarily on a set of microwindows covering the 1690–1730 cm^{-1} spectral range, with additional microwindows in the range 860–880 cm^{-1} used for measurements in the upper troposphere.

In a related study, Gomez et al. [22] have discussed the state of the spectroscopic parameters for HNO_3 for use in retrievals. The data available in the HITRAN [23] and GEISA [24] databases were improved in Ref. [25] in the 11.3 and 8.3 μm regions using new parameters for the line positions [26,27], new line intensity data by Chackerian et al. [28], and a simple empirical model for the air-broadened half-widths [29] to replace the constant default value. While the residuals between atmospheric spectra recorded by MIPAS and those calculated using these new parameters are considerably reduced when compared with results obtained using the previous line parameters available in HITRAN or GEISA, there still are some significant features that can be observed in the residuals. The focus of the Gomez et al. paper was to further investigate nitric acid absorption in order to improve spectra calculations and correct for some of the observed discrepancies. This paper discusses the calculation of the N_2-broadened half-widths that were used in the Gomez et al. paper to replace the simple empirical model. The calculations are based on the complex Robert–Bonamy formalism [30]. First the parameters of the atom–atom component of the isotropic part of the intermolecular potential were adjusted to give better agreement with measured half-widths for the rotation band followed by calculations of the half-width and its temperature dependence for transitions in the ν_5 infrared band.

2. Structure of the HNO_3 infrared spectrum

In its equilibrium configuration, HNO_3 is a C_s-type planar molecule [31]. HNO_3 has nine normal modes ν_i ($i = 1,9$), ν_8 and ν_9 are of A'' symmetry, while the ν_1 to ν_7 modes are of A' symmetry. For this reason, the observed vibrational–rotational transitions are for the following selections rules for transitions between vibrational states $v' = |v_1,\ldots,v_7,v_8,v_9\rangle$ and $v'' = |v_1,\ldots,v_7,v_8,v_9\rangle$: For $\Delta|v_8+v_9| =$ even A- and B-type transitions are observed ($\Delta|K_a| =$ even, $\Delta|K_c| =$ odd) and ($\Delta|K_a| =$ odd, $\Delta|K_c| =$ odd), respectively. This is the case for the ν_5 band, the ν_6 band and the $2\nu_9$ band and also for the $\nu_5+\nu_9-\nu_9$ hot band.

According to the selection rules for an electric dipole moment transition, vibrational bands involving an odd variation of $|\nu_8+\nu_9|$ are C-type bands, while bands with $\Delta|\nu_8+\nu_9| =$ even are hybrid-type bands (i.e. with both A- and B-type transitions). However, the main cold bands appearing in the 11 μm, ν_5 and $2\nu_9$ located at 879.109 and 896.448 cm^{-1}, respectively, which are hybrid in principle, are mostly A-type bands. In order to understand the HNO_3 spectrum, one has to take into account some specific features:

- First, the relative intensities within each band. For HNO_3 A-type bands, the strongest lines involve $[J,K_a,K_c]$ rotational levels with $K_c \sim J$ in the P- and R-branches while for Q-branches only lines with $K_a \sim J$ are actually observable.
- Second, a clustering of rotational levels involving the same J and the same values of K_a or K_c. Indeed, because of the particular values of the rotational constants: nitric acid is an oblate molecule with $A \sim B \sim 2C$ ($A \sim 0.43$ cm^{-1}, $B \sim 0.41$ cm^{-1} and $C \sim 0.20$ cm^{-1} for the $H^{14}N^{16}O_3$ isotopic species) two types of clustering of states occur which correspond to:
  (i) the $[J,K_a = J-K_c,K_c]$ and $[J,K_a = J-K_c+1,K_c]$ rotational levels for $J \geqslant 10$ and $K_a \leqslant J/2$,
  (ii) the $[J,K_a,K_c = J-K_a]$ and $[J,K_a,K_c = J-K_a+1]$ rotational levels for $J \geqslant 15$ and $K_a \geqslant J-2$. In this case K_a may be considered as a "good" quantum number.

Actually the two levels involved in the first type of clustering belong to the same symmetry species in C_s because they involve the same K_c value and the two levels involved in the second type of clustering belong to different symmetry species in C_s because they involve different K_c values.

The effects of these degeneracies on the half-widths and their temperature dependence are discussed below.

3. Complex Robert–Bonamy formalism applied to the HNO_3–N_2 system

The calculations are made using the complex implementation of the Robert–Bonamy (CRB) theory [30]. Here the method is summarized, details of the method can be found in Refs. [32–34]. The calculations are complex valued and yield the pressure-broadened half-width and pressure-induced line shift from a single calculation. Within the CRB formalism the half-width, γ, and line shift, δ, of a ro-vibrational transition $f \leftarrow i$ are given by minus the imaginary part and the real part, respectively, of the diagonal elements of the complex relaxation matrix [35,36]. In computational form the half-width and line shift are usually expressed in terms of the Liouville scattering matrix

$$(\gamma - i\delta) = \frac{n_2}{2\pi c}\langle v[1 - e^{-{}^{R}S_2(f,i,J_2,v,b)}e^{-i{}^{I}S_2(f,i,J_2,v,b)}]\rangle_{v,b,J}, \tag{1}$$

where n_2 is the number density of perturbers and $\langle\rangle_{v,b,J_2}$ represents an average over all trajectories (impact parameter b and initial relative velocity v) and initial rotational state J_2 of the collision partner. $S_2 = {}^{R}S_2 + i{}^{I}S_2$ is the second order terms in the expansion of the scattering matrix, which depends on the ro-vibrational states involved and associated collision induced jumps from these levels, on the intermolecular potential and characteristics of the collision dynamics. Note, Eq. (1) generally contains the vibrational dephasing term, S_1, which arises only for transitions where there is a change in the vibrational state. The potential leading to S_1 is written in terms of the isotropic induction and London dispersion interactions which depend on the vibrational dependence of the dipole moment and polarizability of the radiating molecule. These parameters are not available for HNO_3 and the S_1 term has been omitted from the calculation. Note, the effect of the S_1 term on the half-width often tends to be small. The exact form of the S_2 term is given in Refs. [32–34].

The intermolecular potential used in the calculations is comprised of an electrostatic component (dipole and quadrupole moments of HNO_3 with the quadrupole moment of N_2) and an atom–atom component. The heteronuclear Lennard-Jones parameters for the atomic pairs are determined using the "combination rules" of Hirschfelder et al. [37]. The atom–atom distance, r_{ij} is expressed in terms of the center of mass separation, R, via the expansion in $1/R$ of Sack [38]. Here the formulation of Neshyba and Gamache [39] expanded to eighth order is used. The dynamics of the collision process are based on Robert and Bonamy's second order in time approximation to the true trajectories [30], which gives curved rather than straight line trajectories. These trajectories are based on the isotropic part of the intermolecular potential.

The wavefunctions used to evaluate the reduced matrix elements are obtained by diagonalizing the Watson Hamiltonian [40] in a symmetric top basis. The wavefunctions for the ground vibrational state are determined using the Watson–Hamiltonian constants of Goldman et al. [41] and those for the v_5 vibrational state use the Watson constants of Maki and Wells [42]. The molecular constants for N_2 are from Huber and Herzberg [43].

The molecular parameters for the HNO_3–N_2 system used in this work are as follows: The dipole moment takes the lower limit from the work of Cox and Riveros [44], $\mu = 2.15$ D. The quadrupole moments are from Albinus et al. [45] taken with HNO_3 in the I^R representation: $Q_{xx} = -3.34 \pm 0.23 \times 10^{-26}$ esu, $Q_{yy} = +1.06 \pm 0.33 \times 10^{-26}$ esu, $Q_{zz} = +2.28 \pm 0.23 \times 10^{-26}$ esu. The quadrupole moment of nitrogen is from Mulder et al. [46], $Q_{zz} = -1.4 \pm 0.1 \times 10^{-26}$ esu. The atom–atom parameters were obtained using the standard combination rules with the atom–atom parameters for homonuclear diatomics determined by Bouanich [47] by fitting to second virial coefficient data. These parameters are reported in Table 1. In the calculations, the atom–atom potential is expanded to eight-order in the molecular centers of mass separation.

In the parabolic trajectory approximation the isotropic part of the interaction potential is taken into account in determining the distance, effective velocity, and force at closest approach. To simplify the trajectory calculations the isotropic part of the atom–atom expansion is fit to an isotropic Lennard-Jones 6–12 potential.

The input Lennard-Jones atom–atom parameters are not as well knows as the other parameters; the ε values can vary by 30% and the σ values by 5% depending on the source and the ε values can vary by 69% and the σ values by 9% depending on whether they were derived using viscosity data or virial data [37]. Depending on how the values were derived it is possible to find examples in the literature where the parameters for the same interaction pair differ by factors of 2. Thus it appears reasonable to adjust the atom–atom parameters and/or the resulting trajectory parameters provided there are reliable

Table 1
Values of the heteronuclear atom–atom parameters for the HNO_3–N_2 collision system.

Atomic pair	σ (Å)	ε/k_B (K)
H–N	2.99	20.45
N–N	3.29	37.16
O–N	3.15	43.88

Table 2
The eight measurements of Goyette et al. [48], the initial and final isotropic Lennard-Jones trajectory parameters, and the corresponding half-widths at 296 K.

Trajectory parameters		ε/k_B (K) = 145.25 σ (Å) = 4.170	ε/k_B (K) = 165.00 σ (Å) = 3.117
Transition	γ_{Exp}[a]	$\gamma_{initial}$[a]	γ_{final}[a]
$16_{0\,16} \leftarrow 15_{0\,15}$	0.11966	0.13299	0.12641
$14_{2\,12} \leftarrow 13_{2\,11}$	0.12676	0.13493	0.12832
$13_{3\,10} \leftarrow 12_{3\,9}$[b]	0.13385	0.13346	0.12697
$12_{5\,8} \leftarrow 11_{5\,7}$	0.12650	0.13564	0.12899
$11_{6\,6} \leftarrow 10_{6\,5}$	0.13335	0.13556	0.12885
$24_{8\,16} \leftarrow 24_{8\,17}$	0.11053	0.12590	0.11702
$25_{9\,16} \leftarrow 25_{9\,17}$[b]	0.11915	0.12394	0.11479
$26_{10\,16} \leftarrow 26_{10\,17}$[b]	0.11433	0.12368	0.11427

[a] In units of $cm^{-1}\,atm^{-1}$.
[b] 300 K.

experimental data to fit to. In this work, the trajectories were modified by adjusting the isotropic Lennard-Jones parameters such that the calculations would better agree with measurement. To accomplish this in a reasonable amount of time eight transitions were chosen from the rotation band measurements of Goyette et al. [48]. Rotation band calculations were made and compared with the measured values and the isotropic Lennard-Jones parameters were adjusted until the average percent difference (initially −6.5) was −0.3. This procedure gave final isotropic Lennard-Jones parameters that are 13.6% larger in $\varepsilon/k_B(K)$ and a 25.3% smaller in σ than the initial values. The initial and final parameters and resulting half-widths are given in Table 2.

4. Calculations

The selection of transitions in the ν_5 band to study was made in several stages. First ν_5 band transitions with an intensity greater or equal to $S_{max}/100$ were taken from the HITRAN database [23], where S_{max} is the maximum line intensity in the band. This produced a list of 15 609 transitions. The list was filtered removing all transitions with $J>45$; the resulting list contained 12 553 transitions. To shorten the list of transitions an intensity cutoff of $5.\times10^{-22}\,cm^{-1}/mol\,cm^{-2}$ was applied. This produced a list of 5011 transitions. However, due to limitations in the codes, calculations could not be made for a number of the high J (P- and R-branch) transitions resulting in a final list of 4979 transitions that were studied.

The calculation of the half-width and line shift were made for these transitions of HNO_3 broadened by N_2 at seven temperatures (200., 225., 275., 296., 300., 375., 500. K) by explicitly performing the averaging over the Maxwell–Boltzmann distribution of velocities (Eq. (1)). The intermolecular potential for the calculations is described above. From the eight transitions studied in the optimization of the trajectory parameters, a sense of the magnitude of the line shifts in the rotation band can be obtained. The shifts were both positive and negative and the largest magnitude was 0.97×10^{-3} $cm^{-1}\,atm^{-1}$. The calculations for the ν_5 band transitions did not use the S_1 part of the intermolecular potential, hence the resulting line shifts are not reported.

For applications to atmospheres, the temperature dependence of the half-widths must be known. Theoretical consideration of the temperature dependence of the half-width for a one term intermolecular potential gives the power law model [49],

$$\gamma(T) = \gamma(T_0)\left\{\frac{T_0}{T}\right\}^n, \tag{2}$$

where n is called the temperature exponent.

The temperature exponent was determined for each transition by a least-squares fit of $\ln[\gamma(T)/\gamma(T_0)]$ vs. $\ln[T_0/T]$ using the seven temperatures of the study. The error in the temperature exponent was determined as follows: The temperature exponents were calculated using the half-width values at any two of the temperatures studied. With seven temperatures this yields 21 2-point temperature exponents. The difference between each 2-point temperature exponent and the 7-point fit value is calculated. The error is taken as the largest of these differences. While this procedure tends to yield the maximum error in the temperature exponent, given the nature of the data and other uncertainties it is thought to be more reasonable than a statistical value taken from the fit.

5. Discussion

5.1. Half-width as a function of the rotational quantum numbers

The calculations were made for 4979 transitions in the v_5 band with J'' ranging from 1 to 45 and K_c'' from 0 to 43. At 296 K the half-widths go from a minimum value of 0.0923 cm^{-1} atm^{-1} to a maximum value of 0.1316 cm^{-1} atm^{-1}. The leading electrostatic component for this system is the dipole–quadrupole interaction. With the large dipole moment of HNO_3, $\mu = 2.15$ D, large half-widths are expected. In Fig. 1 the half-width is plotted versus $J''+0.9*(K_c''/J'')$ where the plot symbols are K_c''. The factor that is added to J (abscissa) is to spread points out for a particular J'' value as a function of K_c''. The plot does show some structure. For example, the bottom line of points consists of transitions with $K_c'' = 0$ and 1. Above this, the series of lines are for $K_c'' = 1$ and 2, then $K_c'' = 2$ and 3, etc. After $K_c'' = 3$ the lines blend and for many of the transitions studied there is considerable overlap and any propensity rules are difficult to establish.

To try to better see the structure, plots were made of the N_2-broadened half-width versus the lower rotational state *index* $(J''*(J''+1)+K_a''-K_c''+1)$. This is an energy ordered index, which gives some insight into the associated energy gaps in the collision process. The plots were made (not shown here) in panels for a given J'' of the index running from 1 to 2025 with the $|\Delta K_c| = 1$, 3, and >3 points marked in the plots. The plots show the transitions occur in doublets and are dominated by $|\Delta K_c| = 1$ transitions. What is observed is that for each value of J'' there is a sequence of points (note, the sequence is for $K_c'' = J''$ to $K_c'' = 0$). At low J'' the points have roughly the same half-width for the whole sequence with a slight decrease where $K_c'' = 0$. By $J'' = 8$ the half-widths are decreasing noticeably as K_c'' goes to zero. At around $J'' = 18$ the data have a small decrease for high values of K_c'' followed by an increase in the half-widths as K_c'' decreases, then at $K_c'' \sim 6$ there is a sharp decrease. The trend of the half-width with *index* becomes more evident for larger J'' values. To demonstrate this, the sequence for $J'' = 27$ is plotted in Fig. 2. This corresponds to the *index* running from 730 (27_{027}) to 784 (27_{270}). In the top panel the symbols are an asterisk (*) for the *P*-branch, open circle (O) for the *Q*-branch, and open delta (Δ) for the *R*-branch transitions. For K_c'' large the half-widths for the *R*-branch transitions are the lowest. At *index* = 738 and slightly larger the *Q*-branch half-widths lie between the *R*- and *P*-branch values. The half-width for the *R*-, *Q*-, and *P*-branch transitions steadily increase. At around *index* = 770 the values start to spread but the general trend is for the half-widths

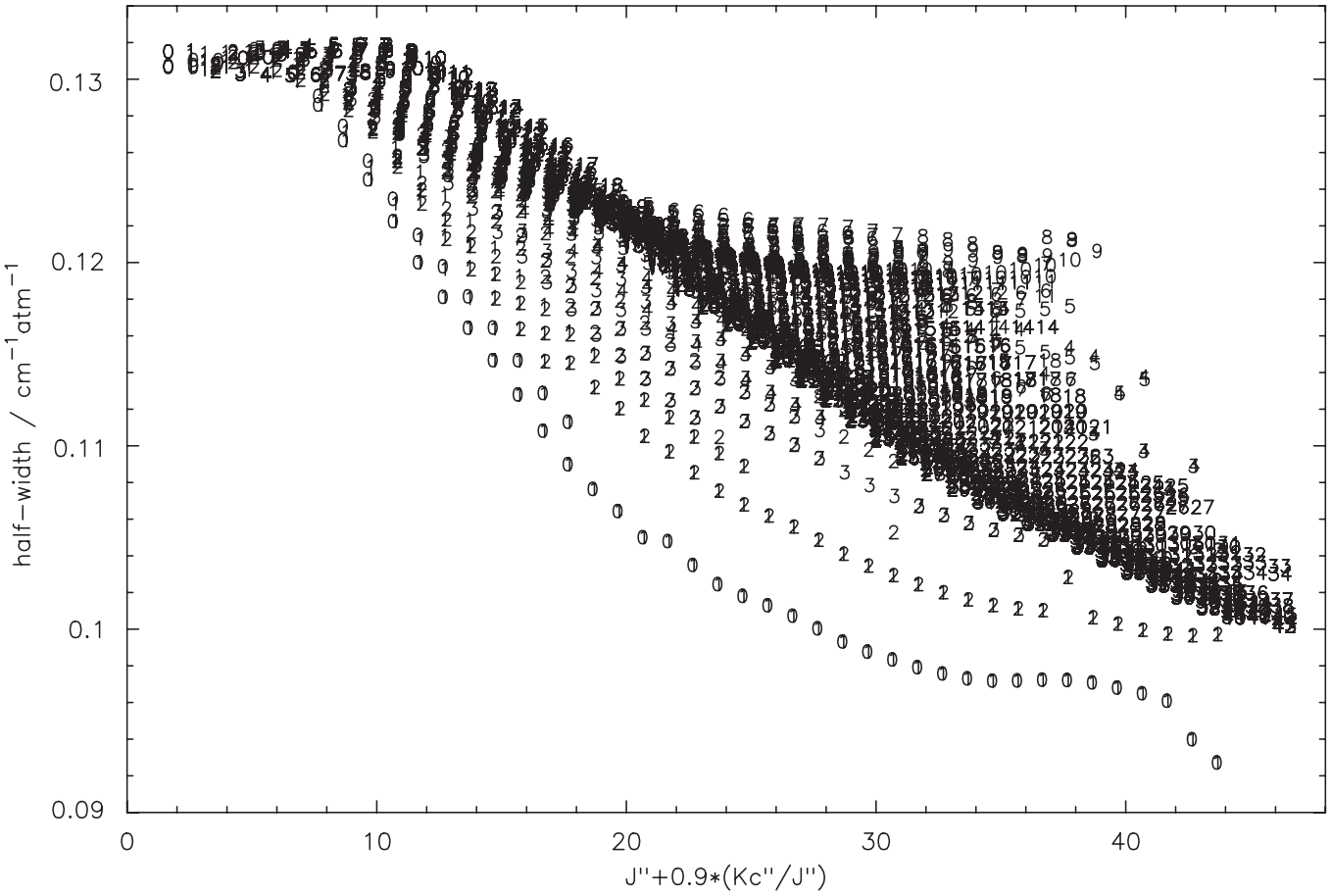

Fig. 1. Calculated N_2-broadened half-widths of v_5 transitions of HNO_3 at 296 K versus $J''+0.9*(K_c''/J'')$. The plot symbols are K_c''.

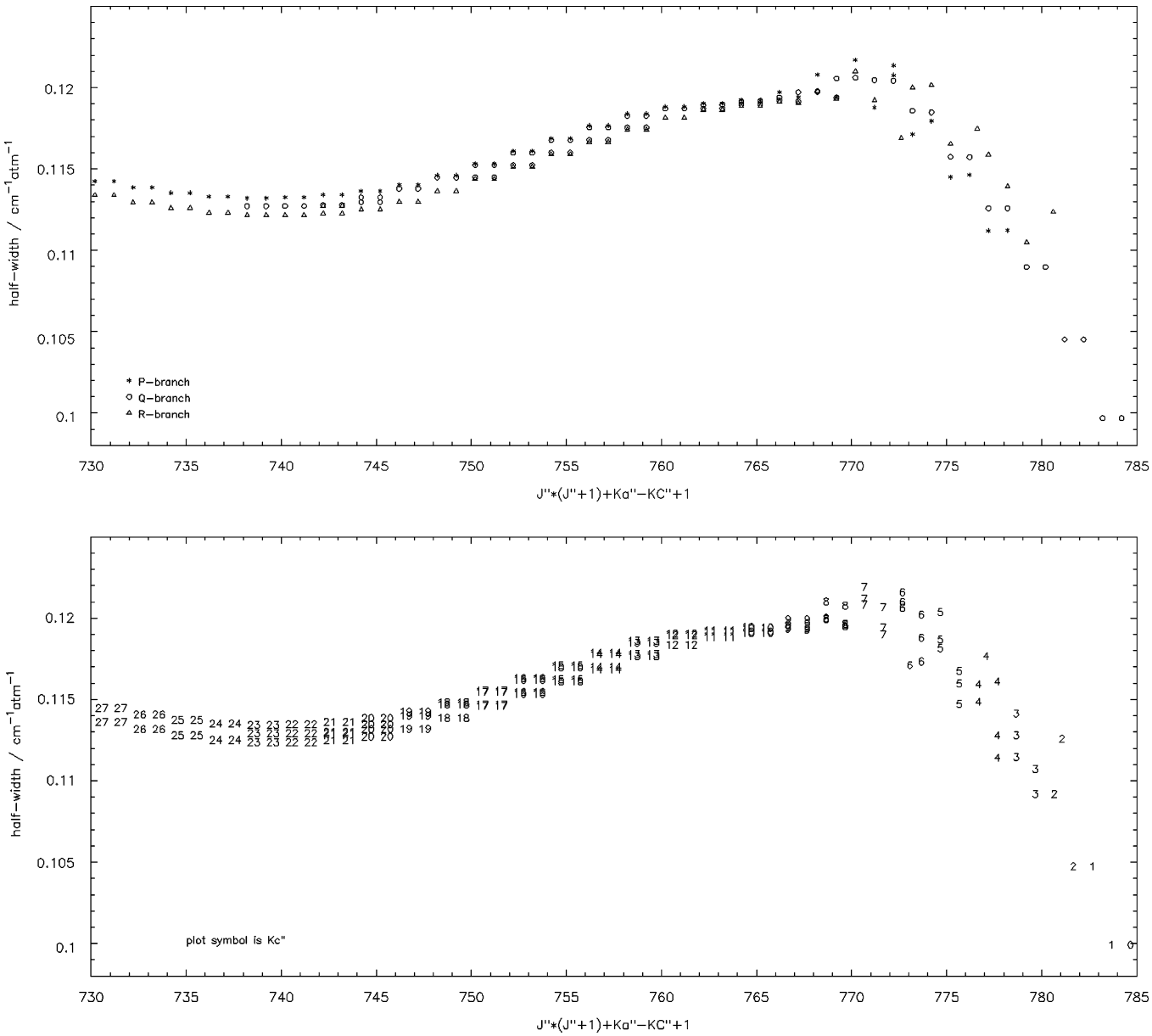

Fig. 2. Top panel: Calculated N_2-broadened half-widths at 296 K for transitions with $J'' = 27$ versus the rotational state *index*, $(J''*(J''+1)+K_a''-K_c''+1)$, plotted are the data for *index* running from 730 (27_{027}) to 784 (27_{270}). The symbols are an asterisk (*) for the *P*-branch, open circle (○) for the *Q*-branch, and open delta (Δ) for the *R*-branch transitions. Bottom panel: Same as above with plot symbols equal to K_c''.

to decrease rapidly beyond this point. Note, for *index* >770 the *P*-branch lines have the smallest half-widths followed by *Q*- and *R*-branch transitions. To understand the structure with respect to K_c'' the lower panel of Fig. 2 is the same data plotted where the plot symbol is K_c'' of the transition.

Table 3 gives the data for the sequence of points for *index* equal 1297 (36_{036}) to 1397 (36_{360}). The data have been sorted on the value of the half-width. The degeneracies discussed above for the line positions and line intensities occur also for the half-widths and their temperature dependence. Indeed, for these degenerate transitions identical values were achieved for the line width parameters (see Table 3).

5.2. Vibrational dependence of the half-width

Half-widths for 300 v_5 transitions were compared with the computed half-width for the corresponding rotation band transitions to obtain some sense of the vibrational dependence of the half-width. We caution that because we do not have the molecular parameters needed for the S_1 term the comparison will only be for the spectroscopic effects (energies,

Table 3
Calculated half-widths at 296 K and their temperature dependence for the sequence of transitions with *index* running from 1297 ($36_{0\,36}$) to 1397 ($36_{36\,0}$).

$J'K_a'K_c'$	$J''K_a''K_c''$	γ ($cm^{-1}\,atm^{-1}$)	n
$35_{d\,35}$	$36_{d\,36}$	105.64	0.751(0.060)
$37_{d\,37}$	$36_{d\,36}$	105.05	0.753(0.064)
$35_{d\,34}$	$36_{d\,35}$	105.41	0.753(0.065)
$37_{d\,36}$	$36_{d\,35}$	104.89	0.756(0.069)
$37_{d\,35}$	$36_{d\,34}$	104.81	0.759(0.073)
$35_{2\,33}$	$36_{2\,34}$	105.38	0.757(0.069)
$35_{d\,32}$	$36_{d\,33}$	105.41	0.761(0.073)
$37_{d\,34}$	$36_{d\,33}$	104.79	0.763(0.077)
$35_{d\,31}$	$36_{d\,32}$	105.51	0.765(0.077)
$37_{d\,33}$	$36_{d\,32}$	104.82	0.766(0.080)
$35_{d\,30}$	$36_{d\,31}$	105.66	0.768(0.079)
$37_{d\,32}$	$36_{d\,31}$	104.93	0.769(0.082)
$35_{d\,29}$	$36_{d\,30}$	105.86	0.772(0.081)
$37_{d\,31}$	$36_{d\,30}$	105.12	0.773(0.084)
$35_{d\,28}$	$36_{d\,29}$	106.12	0.777(0.083)
$37_{d\,30}$	$36_{d\,29}$	105.39	0.778(0.086)
$35_{d\,27}$	$36_{d\,28}$	106.46	0.782(0.084)
$37_{d\,29}$	$36_{d\,28}$	105.72	0.783(0.088)
$35_{d\,26}$	$36_{d\,27}$	106.85	0.787(0.086)
$37_{d\,28}$	$36_{d\,27}$	106.10	0.789(0.090)
$35_{d\,25}$	$36_{d\,26}$	107.28	0.793(0.087)
$37_{d\,27}$	$36_{d\,26}$	106.55	0.794(0.091)
$35_{d\,24}$	$36_{d\,25}$	107.78	0.798(0.088)
$37_{d\,26}$	$36_{d\,25}$	107.10	0.800(0.091)
$35_{d\,23}$	$36_{d\,24}$	108.38	0.806(0.089)
$37_{d\,25}$	$36_{d\,24}$	107.70	0.805(0.091)
$35_{d\,22}$	$36_{d\,23}$	109.09	0.815(0.091)
$37_{d\,24}$	$36_{d\,23}$	108.35	0.813(0.092)
$35_{d\,21}$	$36_{d\,22}$	109.87	0.825(0.093)
$37_{d\,23}$	$36_{d\,22}$	109.08	0.822(0.093)
$35_{d\,20}$	$36_{d\,21}$	110.67	0.835(0.094)
$37_{d\,22}$	$36_{d\,21}$	109.87	0.832(0.095)
$35_{d\,19}$	$36_{d\,20}$	111.51	0.845(0.096)
$37_{d\,21}$	$36_{d\,20}$	110.70	0.842(0.097)
$37_{d\,20}$	$36_{d\,19}$	111.55	0.852(0.099)
$35_{19\,17}$	$36_{18\,18}$	113.30	0.867(0.100)
$37_{18\,19}$	$36_{18\,18}$	112.42	0.863(0.100)
$35_{20\,15}$	$36_{19\,18}$	114.30	0.878(0.101)
$37_{19\,19}$	$36_{19\,18}$	112.42	0.863(0.100)
$37_{19\,18}$	$36_{20\,17}$	113.30	0.872(0.101)
$37_{23\,15}$	$36_{22\,14}$	116.13	0.901(0.102)
$37_{22\,15}$	$36_{23\,14}$	116.13	0.901(0.102)
$37_{24\,14}$	$36_{25\,11}$	117.83	0.914(0.100)
$37_{25\,12}$	$36_{26\,11}$	118.62	0.921(0.100)
$37_{26\,11}$	$36_{26\,10}$	119.52	0.925(0.097)
$37_{27\,11}$	$36_{27\,10}$	118.90	0.924(0.099)
$37_{26\,12}$	$36_{27\,9}$	120.04	0.927(0.096)
$37_{28\,9}$	$36_{28\,8}$	121.04	0.933(0.091)
$37_{29\,8}$	$36_{29\,7}$	119.58	0.930(0.097)
$36_{33\,4}$	$36_{30\,7}$	112.40	0.922(0.120)
$36_{33\,3}$	$36_{30\,6}$	112.50	0.922(0.120)
$36_{27\,9}$	$36_{31\,6}$	118.11	0.927(0.103)
$36_{26\,10}$	$36_{31\,5}$	117.12	0.924(0.105)
$36_{29\,8}$	$36_{32\,5}$	114.76	0.923(0.113)
$36_{30\,7}$	$36_{32\,4}$	113.59	0.922(0.116)
$36_{32\,d}$	$36_{33\,d}$	109.50	0.920(0.129)
$36_{34\,d}$	$36_{34\,d}$	104.54	0.916(0.143)
$36_{35\,d}$	$36_{35\,d}$	100.68	0.915(0.156)
$36_{36\,d}$	$36_{36\,d}$	96.89	0.915(0.171)

In the K_a columns (resp. K_c columns), the letter "d" stands for degenerate K_a values, with $K_a = J-K_c$ and $K_a = J-K_c+1$ (resp. for degenerate K_c values with $K_c = J-K_a$ and $K_c = J-K_a+1$).

wavefunctions, etc.) and not for effects of the vibrational dephasing term. The transitions ranged from $J = 8$ to 14 and were randomly selected. The comparison showed very small percent differences between the results for the two bands, generally between 0.01% and 0.02%. Note, it is the difference in energy from a state i to i' that enters the calculation and not the energy. Thus the spectroscopic part of the vibrational dependence is exceedingly small for the HNO_3–N_2 system.

5.3. Temperature dependence of the half-width

The temperature dependence of the half-width was determined for the 4979 v_5 transitions studied in this work using the power law formula, Eq. (2). A "rule-of-thumb" expression for the temperature exponent has been given by Birnbaum [49], which for a "dipole–quadrupole" system, such as HNO_3–N_2, gives 5/6. Chu et al. [50] have studied the effect of changing the temperature exponent on retrieved mixing ratios of water vapor. They find that changing n from 0.5 to 0.7 results in roughly a 4% change in the mixing ratio at 10 km. It has also been demonstrated that temperature exponents averaged as a function of J'' or fit by polynomials in the rotational quantum numbers do not give reliable predictions for all transitions [51,52]. Given the results of Chu et al. it is clear that the use of the specific measured or calculated temperature exponent for the ro-vibrational transition in question will yield the best results.

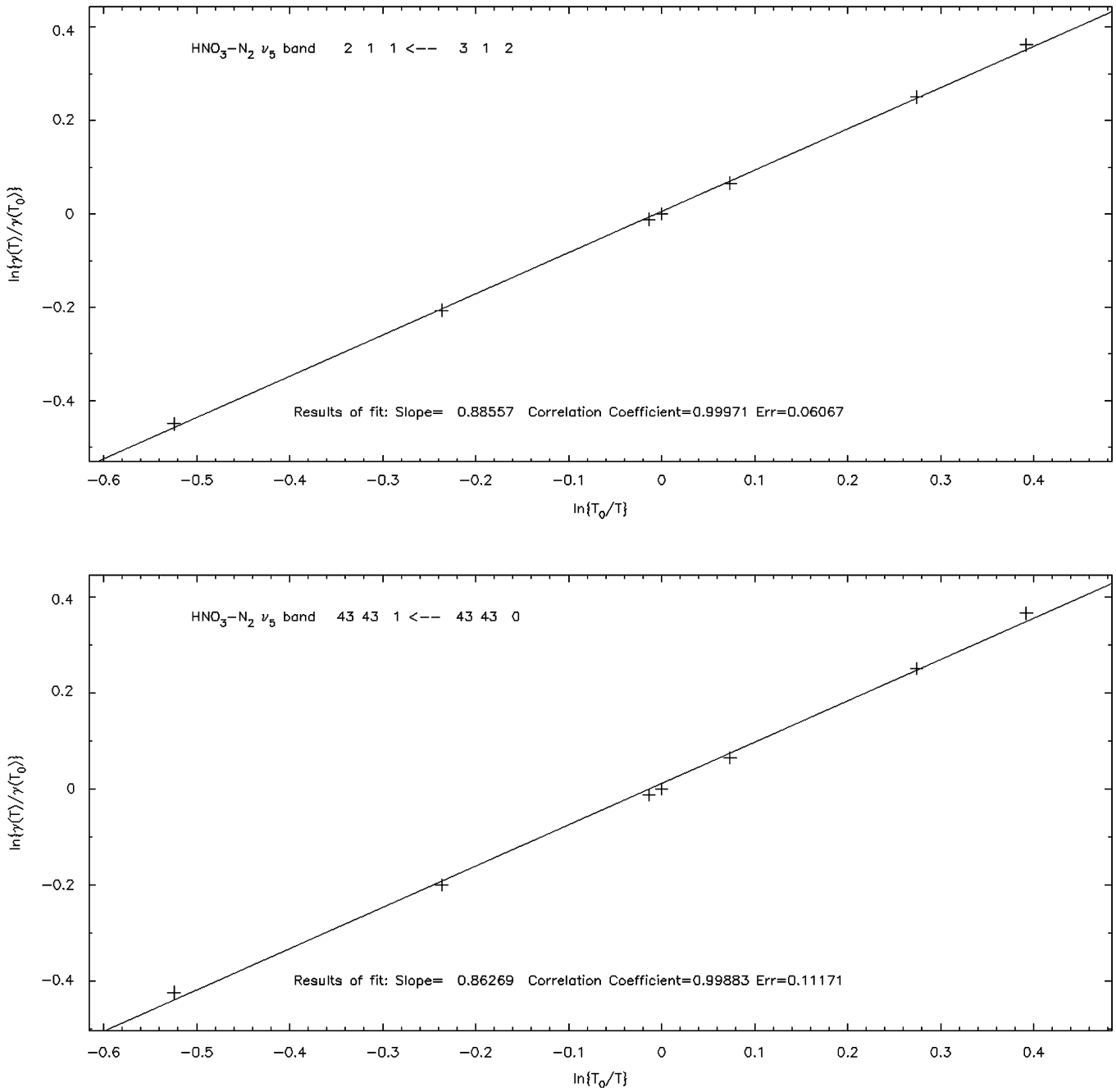

Fig. 3. $\ln[\gamma(T)/\gamma(T_0)]$ versus $\ln[T_0/T]$; data are for N_2-broadening of v_5 transitions, the top panel is for the $2_{11} \leftarrow 3_{12}$ transition and the bottom panel is for the $43_{431} \leftarrow 43_{430}$ transition.

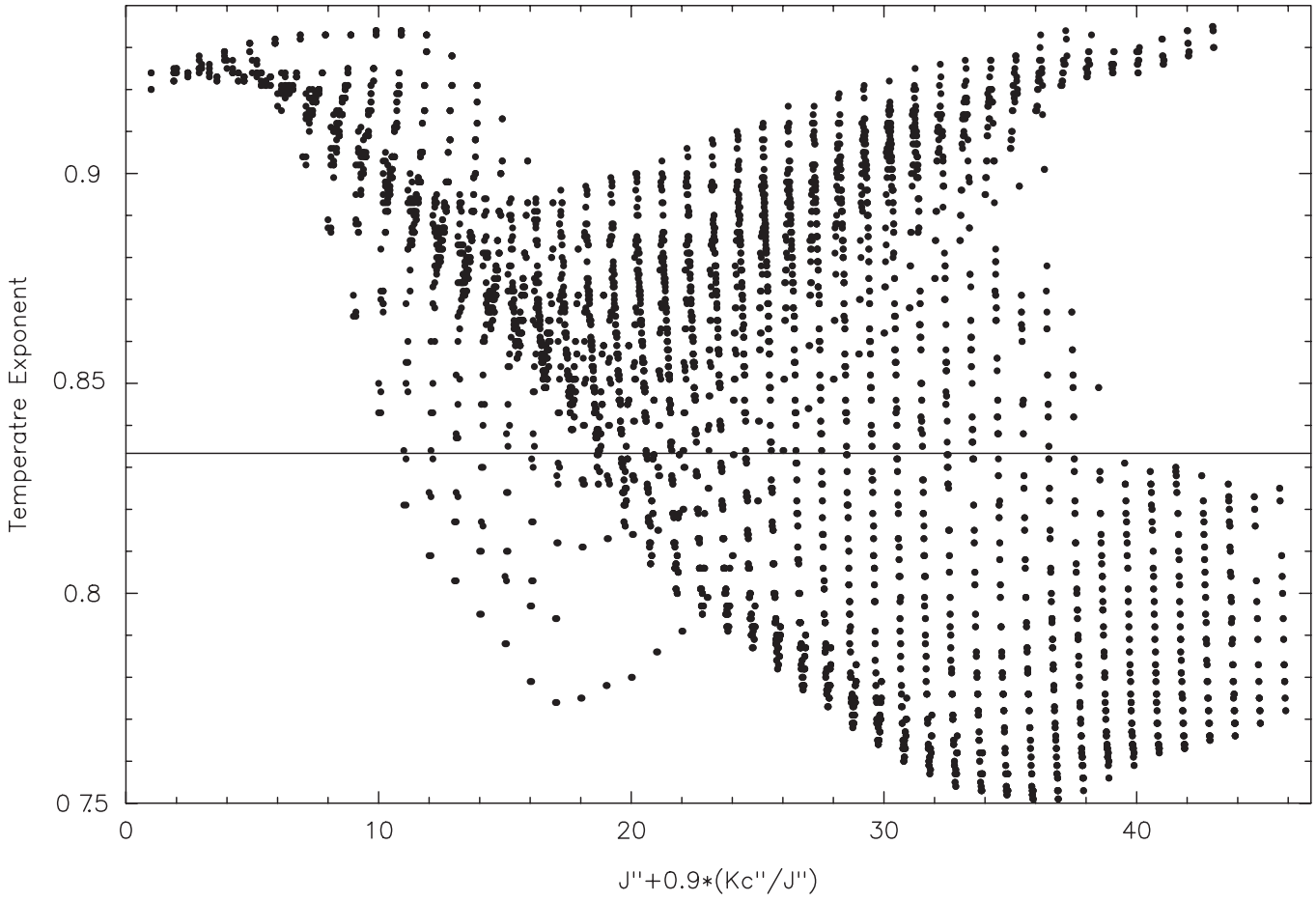

Fig. 4. Temperature exponents for N_2-broadening of 4979 ν_5 transitions of HNO_3 versus $J''+0.9^*(K_c''/J'')$. Solid horizontal line is the dipole–quadrupole "rule-of-thumb" value, 5/6.

Some recent studies have shown that for certain types of radiator–perturber interactions the power law model is questionable. Wagner et al. [53] have observed that for certain transitions of water vapor perturbed by air, N_2 or O_2 the power law does not correctly model the temperature dependence of the half-width. This fact was also demonstrated by Toth et al. [54] in a study of air-broadening of water vapor transitions in the region from 696 to 2163 cm^{-1}. In both studies it was found that the temperature exponent, n, can be negative for many transitions. In such cases the power law model, Eq. (2), is not valid. The mechanism leading to negative temperature exponents is called the resonance overtaking effect and was discussed by Wagner et al. [53], Antony et al. [55] and Hartmann et al. [56]. Thus, in this work the applicability of the power law model was tested.

Fig. 3 shows the results of the least-squares fit to the data, straight line, to determine n. Plotted are $\ln[\gamma(T)/\gamma(T_0)]$ versus $\ln[T_0/T]$, where the top panel is for the $2_{11}\leftarrow3_{12}$ transition and the bottom panel is for the $43\ _{431}\leftarrow43\ _{430}$ transition. The reference temperature, T_0, was takes as 296 K. Note, in the figures that temperature is increasing from right to left. Both panels show that the fit line does not pass through all the points, indicating a better approximation for the temperature dependence may be needed, such as a double power law model [57]. However, for the transitions studied here the power law gives a reasonable description of the temperature dependence of the N_2-broadened half-width over the range $T = 200$–500 K, suggesting the major contributions to the half-widths are from the $Re(S_2)$ terms [55].

Fig. 4 shows the temperature exponent for N_2-broadening of HNO_3 versus $J''+0.9^*(K_c''/J'')$ for the 4979 transitions studied here. The solid line at 5/6 is the "rule-of-thumb" value. The n values do not show large variation and range about $\pm10\%$ about the "rule-of-thumb" value. There appears to be structure in the figure but with so many transitions it is difficult to obtain insight of how the temperature exponent might depend on the quantum numbers.

In Fig. 5 the temperature exponent is plotted versus $J''+0.9^*(K_c''/J'')$ for the P-branch (top panel), Q-branch (middle panel), and R-branch (bottom panel) for only the $|\Delta K_c| = 1$ transitions. The plot symbols used in the graph are K_c'' of the transition. The straight line is the "rule-of-thumb" value. For this subset of transitions, patterns can be seen. The temperature exponent for a given K_c'' changes smoothly as a function of $J''+0.9^*(K_c''/J'')$. For J'' less than ~20, at a fixed J'' n is largest for $K_c'' = J''$ and decreases as K_c'' decreases. After J''~20 the situation is reversed and n decreases as K_c'' increases. For other choices of $|\Delta K_c|$ the patterns are not as clear.

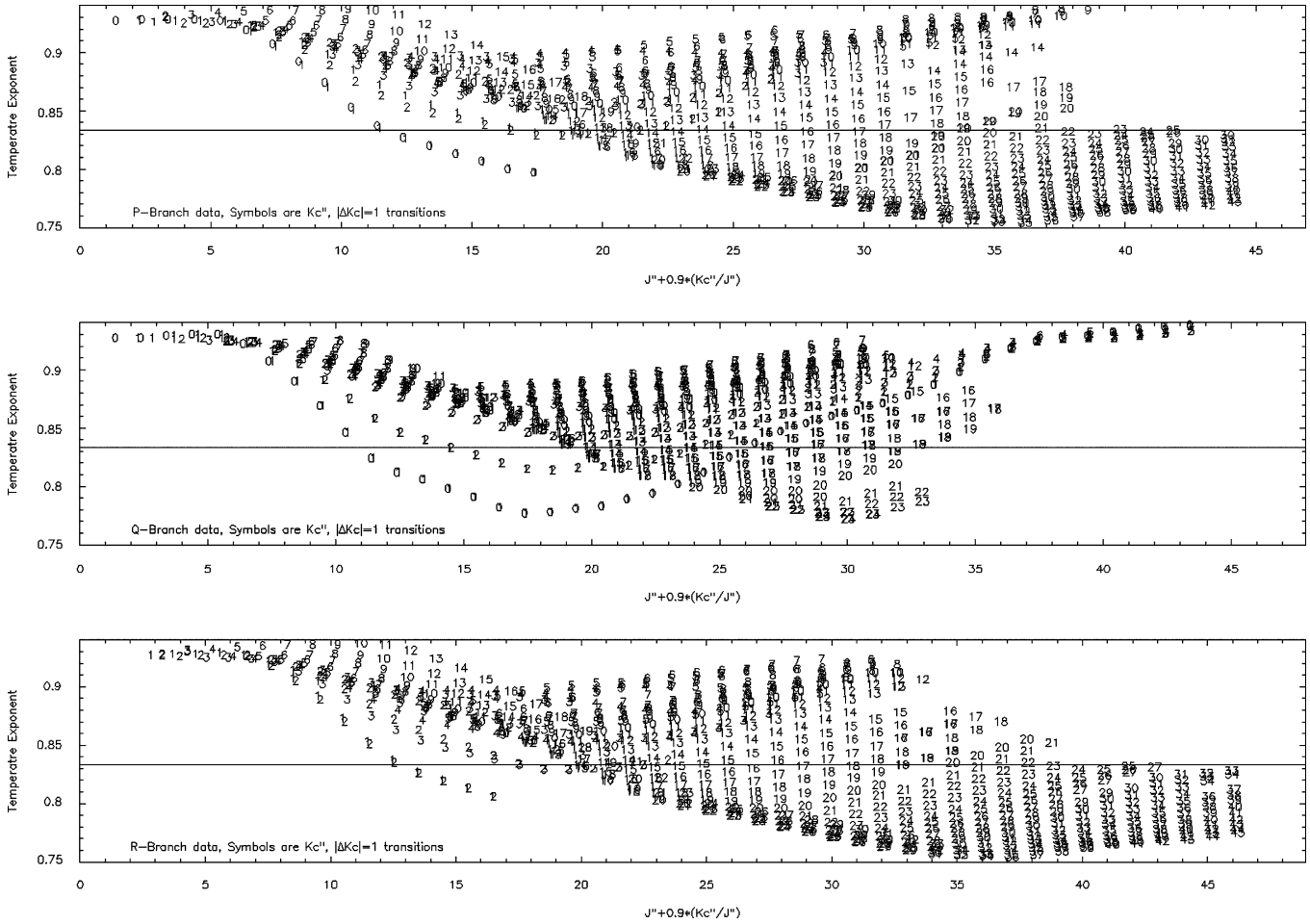

Fig. 5. Temperature exponent versus $J''+0.9^{*}(K_c''/J'')$ for the *P*-branch (top panel), *Q*-branch (middle panel), and *R*-branch (bottom panel) for the $|\Delta K_c| = 1$ transitions. The plot symbols are K_c''. Solid horizontal line is the dipole–quadrupole "rule-of-thumb" value, 5/6.

5.4. Comparison with measurements

To our knowledge there have been no line shape measurements made on nitric acid in the infrared region of the spectrum. A number of the groups made measurements of nitrogen- and oxygen-broadening of HNO_3 rotation band transitions [48,58–61] allowing the air-broadening value to be determined for 33 lines. The ratio of air to nitrogen broadening can then be taken for these data points. This procedure yields an average ratio of 0.936 (close to the value used in Ref. [22]) with a minimum value of 0.897 and a max value of 0.961. This ratio was used to compare our N_2-broadened calculations to air-broadening measurements.

There have been 38 measurements of N_2-broadening of HNO_3 [48,58–61] of which six transitions have been measured by two groups. Ref. [62] reports measurements of air-broadening of seven rotation band lines of HNO_3. These data are for transitions with J' ranging from 10 to 44. The N_2- and air-broadened measurements along with the corresponding CRB calculated value are given in Table 4 ordered by J'' in the list. Fig. 6 shows the N_2-broadened (solid triangle symbols, ▲) and air-broadened (solid square symbols, □) measurements with 2-sigma error bars, and the CRB calculated (N_2-broadened or scaled to air by 0.936) values (⊕ symbols) versus the line number. The average percent difference between the N_2-broadening measurements and calculations is −2.38% with a standard deviation of 5.6%. Comparing the seven air-broadened measurements of Cazzoli et al. to the N_2-broadened CRB calculations scaled by 0.936 gives an average percent difference of −0.65 and a standard deviation of 2.5.

Refs. [48,60,61] report the temperature dependence of the N_2-broadened half-width for 10 transitions for which calculations were made. The measurements range from 0.57 to 0.88. The calculations give a narrower range, 0.78–0.89, and the average percent difference between the measurements and calculations is 22.

6. Conclusions

Complex Robert–Bonamy calculations of the nitrogen-broadened half-widths for 4979 transitions of the ν_5 band of HNO_3 have been made at seven temperatures from 200 to 500 K. From these data the temperature dependence of the

Table 4
Measured N_2- and air-broadened half-widths and the corresponding CRB calculated value at 296 K.

Line	Perturber	$J'_{K'_aK'_c}$	$J''_{K''_aK''_c}$	γ_{Exp}[a]	Ref.	γ_{CRB}[a]
1	N_2	$11_{6\,6}$	$10_{6\,5}$	0.11712	[59]	0.12848
2	N_2	$11_{9\,3}$	$10_{9\,2}$	0.13297	[48]	0.12546
3	N_2	$12_{6\,6}$	$11_{6\,5}$	0.13436	[59]	0.12724
4	N_2	$12_{5\,8}$	$11_{5\,7}$	0.12673	[48]	0.12863
5	N_2	$13_{11\,2}$	$12_{11\,1}$	0.12346	[59]	0.12329
6	N_2	$13_{3\,10}$	$12_{3\,9}$	0.13298	[48]	0.12846
7	N_2	$14_{8\,6}$	$13_{8\,5}$	0.12371	[59]	0.12503
8	N_2	$14_{2\,12}$	$13_{2\,11}$	0.12977	[48]	0.12797
8	N_2	$14_{2\,12}$	$13_{2\,11}$	0.13350	[61]	0.12797
9	N_2	$14_{4\,10}$	$13_{4\,9}$	0.12574	[59]	0.12712
10	N_2	$14_{3\,12}$	$14_{3\,11}$	0.13282	[61]	0.12736
11	air	$15_{13\,3}$	$14_{13\,2}$	0.11595	[62]	0.11231[b]
12	N_2	$16_{0\,16}$	$15_{0\,15}$	0.12179	[48]	0.12607
13	N_2	$18_{0\,18}$	$17_{0\,17}$	0.11585	[59]	0.12386
13	N_2	$18_{0\,18}$	$17_{0\,17}$	0.12040	[60]	0.12386
14	N_2	$18_{12\,7}$	$17_{12\,6}$	0.12092	[59]	0.12244
15	N_2	$19_{3\,16}$	$18_{3\,15}$	0.11636	[59]	0.12174
16	N_2	$20_{15\,5}$	$19_{15\,4}$	0.09887	[59]	0.12277
17	N_2	$22_{7\,15}$	$21_{7\,14}$	0.11712	[59]	0.11929
17	N_2	$22_{7\,15}$	$21_{7\,14}$	0.11547	[60]	0.11929
18	N_2	$22_{0\,22}$	$21_{0\,21}$	0.10622	[59]	0.11899
19	N_2	$24_{13\,11}$	$23_{14\,10}$	0.11407	[61]	0.11971
20	N_2	$24_{8\,16}$	$24_{8\,17}$	0.11518	[48]	0.11670
21	air	$25_{0\,25}$	$24_{0\,24}$	0.10627	[62]	0.10847[b]
22	N_2	$25_{9\,16}$	$25_{9\,17}$	0.11904	[48]	0.11558
23	N_2	$26_{9\,17}$	$25_{9\,16}$	0.11154	[59]	0.11564
24	N_2	$26_{10\,16}$	$26_{10\,17}$	0.11514	[48]	0.11545
25	air	$26_{1\,25}$	$26_{0\,26}$	0.10675	[62]	0.10719[b]
26	air	$27_{0\,27}$	$26_{0\,26}$	0.10517	[62]	0.10695[b]
27	N_2	$27_{9\,18}$	$26_{9\,17}$	0.10825	[59]	0.11459
28	air	$27_{2\,25}$	$27_{1\,26}$	0.10855	[62]	0.10601[b]
29	N_2	$29_{0\,29}$	$28_{0\,28}$	0.10216	[59]	0.11250
29	N_2	$29_{0\,29}$	$28_{0\,28}$	0.10743	[60]	0.11250
30	N_2	$30_{14\,16}$	$30_{14\,17}$	0.11410	[58]	0.11450
31	N_2	$31_{22\,9}$	$30_{22\,8}$	0.11260	[58]	0.12046
32	N_2	$32_{23\,10}$	$31_{23\,9}$	0.11330	[58]	0.11907
33	N_2	$32_{28\,5}$	$31_{28\,4}$	0.11990	[58]	0.11125
34	N_2	$32_{28\,4}$	$31_{28\,3}$	0.10570	[58]	0.11126
35	N_2	$35_{0\,35}$	$34_{0\,34}$	0.10340	[58]	0.10646
35	N_2	$35_{0\,35}$	$34_{0\,34}$	0.10343	[59]	0.10646
36	N_2	$36_{0\,36}$	$35_{0\,35}$	0.10670	[58]	0.10562
36	N_2	$36_{0\,36}$	$35_{0\,35}$	0.10673	[59]	0.10562
37	N_2	$38_{5\,33}$	$37_{5\,32}$	0.10545	[61]	0.10421
38	air	$43_{18\,25}$	$43_{17\,26}$	0.09684	[62]	0.09984[b]
39	air	$44_{19\,25}$	$44_{18\,26}$	0.09714	[62]	0.09983[b]

[a] In units of $cm^{-1}\,atm^{-1}$.
[b] Scaled to air-broadening by $0.936^{*}\gamma(N_2)$.

half-width has been determined for each transition. The results show that the power law model of the temperature dependence of the half-width works well for this collision system. Comparison of the calculated N_2-broadened half-widths and calculated N_2-broadened half-widths scaled to air-broadening with the measured values show very good agreement.

The half-widths determined in this work were scaled to air-broadening by multiplying them by 0.935 and used in simulations [22]. While improved agreement with measured spectra was observed (see Ref. [22] for details), scaling can introduce error on the order of $\pm 4\%$. Calculations of O_2-broadened half-widths for the 4979 transitions of the ν_5 band of HNO_3 studied in this work would eliminate this error. These calculations will be pursued in the future.

Because little vibrational dependence was found for the half-widths for the HNO_3–N_2 collision system the calculations presented here can be used for these cases.

The N_2-broadened half-widths and temperature dependence of the half-width determined in this work are available at the web site of one of the authors (faculty.uml.edu/Robert_Gamache) and the air-broadened half-width and temperature exponent are in the supplementary data of Ref. [22].

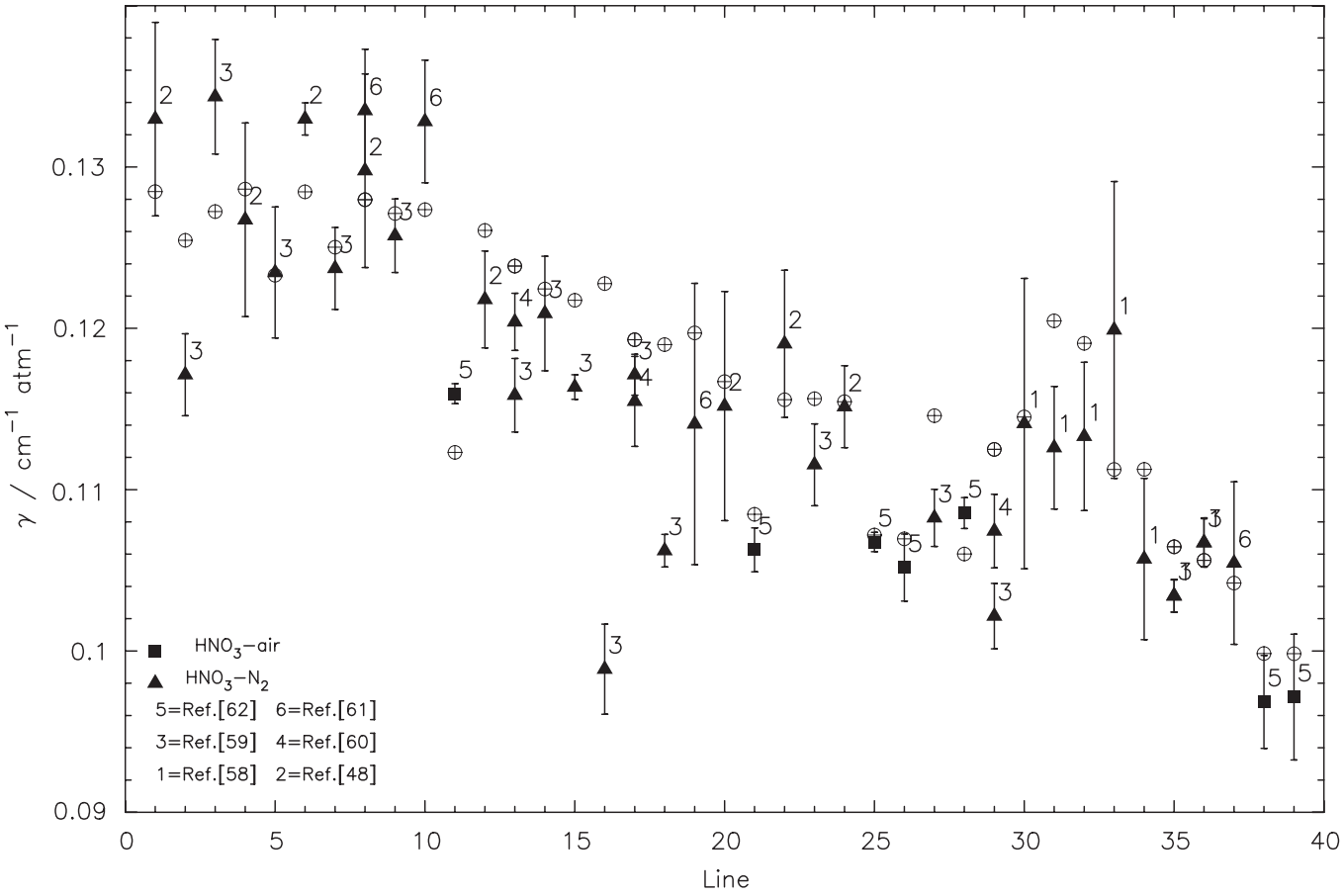

Fig. 6. N_2-broadened (solid triangle symbols, ▲) and air-broadened (solid square symbols, □) measurements with 2-sigma error bars, and the CRB calculated (N_2-broadened or scaled to air by 0.936) values (⊕ symbols) versus the line count. Half-widths are in units of $cm^{-1}\,atm^{-1}$ at 296 K.

Acknowledgments

RRG and AL are pleased to acknowledge support of this research by the National Science Foundation through Grant no. ATM-0803135. Any opinions, findings, and conclusions or recommendations expressed in this material are those of the author(s) and do not necessarily reflect the views of the National Science Foundation.

References

[1] Solomon S. Stratospheric ozone depletion: a review of concepts and history. Rev Geophys 1999;37:275–316.
[2] Santee ML, Manney GL, Froidevaux L, Read WG, Waters JW. Six years of UARS Microwave Limb Sounder HNO_3 observations: seasonal, interhemispheric, and interannual variations in the lower stratosphere. J Geophys Res 1999;104:8225–46.
[3] Santee ML, Manney GL, Livesey NJ, Read WG. Three dimensional structure and evolution of stratospheric HNO_3 based on UARS microwave limb sounder measurements. J Geophys Res 2004;109:D15306.
[4] Crutzen PJ. Ozone production rates in oxygen–hydrogen–nitrogen oxide atmosphere. J Geophys Res 1971;78:7311.
[5] Johnston HS. Reduction of stratospheric ozone by nitrogen oxide catalysts from supersonic transport exhaust. Science 1971;173:517–22.
[6] Coffey MT, Hannigan JW, Goldman A, Kinnison D, Gille JC, Barnett JJ, et al. Airborne Fourier transform spectrometer observations in support of EOS Aura validation. J Geophys Res 2008;113:D16S42.
[7] Waters JW, Froidevaux L, Harwood RS, Jarnot RF, Pickett HM, Read WG, et al. The Earth observing system microwave limb sounder (EOS MLS) on the aura satellite. IEEE Trans Geosci Remote Sens 2006;44:1075–92.
[8] Gille J, Barnett J, Arter P, Barker M, Bernath P, Boone C, et al. High Resolution Dynamics Limb Sounder: experiment overview, recovery, and validation of initial temperature data. J Geophys Res 2008;113:D16S43.
[9] Beer R. TES on the aura mission: scientific objectives, measurements, and analysis overview. IEEE Trans Geosci Remote Sens 2006;44:1102–5.
[10] Kinnison DE, Gille JC, Barnett JJ, Randall CE, Harvey VL, Lambert A, et al. Global observations of HNO_3 from the high resolution dynamics limb sounder (HIRDLS)-first results. J Geophys Res 2008;113.
[11] Santee ML, Lambert A, Read WG, Livesey NJ, Cofield RE, Cuddy DT, et al. Validation of the Aura Microwave Limb Sounder HNO_3 measurements. J Geophys Res 2007;112:D24S40.
[12] Toon GC. The JPL MkIV interferometer. Opt Photon News 1991;2:19–21.
[13] Jucks KW, Johnson DG, Chance KV, Traub WA, Salawitch RJ. Nitric acid in the middle stratosphere as a function of altitude and aerosol loading. J Geophys Res 1999;104:26715–23.
[14] Stachnik RA, Salawitch R, Engel A, Schmidt U. Measurements of chlorine partitioning in the winter Arctic stratosphere. Geophys Res Lett 1999;26:3093–6.
[15] Scheuer E, Talbot RW, Dibb JE, Seid GK, DeBell L, Lefer B. Seasonal distributions of fine aerosol sulfate in the North American Arctic basin during TOPSE. J Geophys Res 2003;108.

[16] Neumen JA, Gao RS, Fahey DW, Holecek JC, Ridley BA, Walega JG, et al. In situ measurements of HNO_3, NO_y, NO, and O_3 in the lower stratosphere and upper troposphere. Atmos. Environ 2001;35:5789–97.
[17] Fischer H, Oelhaf H. Remote sensing of vertical profiles of atmospheric trace constituents with MIPAS limb-emission spectrometers. Appl Opt 1996;35:2787–96.
[18] Fischer H, Birk M, Blom C, Carli B, Carlotti M, von Clarmann T, et al. MIPAS: an instrument for atmospheric and climate research. Atmos Chem Phys Discuss 2007;7:8795–893.
[19] Murtagh D, Frisk U, Merino F, Ridal M, Jonsson A, Stegman J, et al. An overview of the Odin atmospheric mission. Can J Phys 2002;80:309–19.
[20] Irie H, Kondo Y, Koike M, Danilin MY, Camy-Peyret C, Payan S, et al. Validation of NO_2 and HNO_3 measurements from the Improved Limb Atmospheric Spectrometer (ILAS) with the version 5.20 retrieval algorithm. J Geophys Res 2002;107:8206.
[21] Bernath PF, McElroy CT, Abrams MC, Boone CD, Butler M, Camy-Peyret C, et al. Atmospheric chemistry experiment (ACE): mission overview. Geophys Res Lett 2005;32:L15S01.
[22] Gomez L, Tran H, Perrin A, Gamache RR, Laraia A, Orphal J, et al. Some improvements of the HNO_3 spectroscopic parameters in the spectral region from 600 to 950 cm^{-1}. J Quant Spectrosc Radiat Transfer 2008; in press, doi:10.1016/j.jqsrt.2008.07.004.
[23] Rothman LS, Jacquemart D, Barbe A, Benner DC, Birk M, Brown LR, et al. The HITRAN 2004 molecular spectroscopic database. J Quant Spectrosc Radiat Transfer 2005;96:139–204.
[24] Jacquinet-Husson N, Arié E, Ballard J, Barbe A, Bjoraker G, Bonnet B, et al. The 1997 spectroscopic GEISA databank. J Quant Spectrosc Radiat Transfer 1999;62:205–54.
[25] Flaud J-M, Brizzi G, Carlotti M, Perrin A, Ridolfi M. MIPAS database: validation of HNO_3 line parameters using MIPAS satellite measurements. Atmos Chem Phys 2006;6:5037–48.
[26] Perrin A, Flaud J-M, Keller F, Goldman A, Blatherwick RD, Murcray FJ, et al. Analysis of the ν_8+ν_9 band of HNO_3: line positions and intensities, and resonances involving the $\nu_6 = \nu_7 = 1$ dark state. J Mol Spectrosc 1999;194:113–23.
[27] Perrin A, Orphal J, Flaud J-M, Klee S, Mellau G, Mäder H, et al. New analysis of the ν_5 and $2\nu_9$ bands of HNO_3 by infrared and millimeter wave techniques: line positions and intensities. J Mol Spectrosc 2004;228:375–91.
[28] Chackerian C, Sharpe SW, Blake TA. Anhydrous nitric acid integrated absorption cross sections: 820–5300 cm^{-1}. J Quant Spectros Radiat Transfer 2003;82:429–41.
[29] Perrin A, Puzzarini C, Colmont J-M, Verdes C, Wlodarczak G, Cazzoli G, et al. Molecular line parameters for the "MASTER" (millimeter wave acquisitions for stratosphere/troposphere exchange research) database. Atmos Chem 2005;51:161–205.
[30] Robert D, Bonamy J. Short range force effects in semiclassical molecular line broadening calculations. J Phys 1979;20:923–43.
[31] Perrin A. Recent progress in the analysis of HNO_3 spectra. Spectrochim Acta A 1998;54:375–93.
[32] Lynch R. Half-widths and line shifts of water vapor perturbed by both nitrogen and oxygen. PhD dissertation, University of Massachusetts Lowell, June 1995.
[33] Gamache RR, Lynch R, Neshyba SP. New developments in the theory of pressure-broadening and pressure-shifting of spectral lines of H_2O: the complex Robert–Bonamy formalism. J Quant Spectrosc Radiat Transfer 1998;59:319–35.
[34] Lynch R, Gamache RR, Neshyba SP. N_2 and O_2 induced half-widths and line shifts of water vapor transitions in the (3 0 1)←(0 0 0) and (2 2 1)←(0 0 0) bands. J Quant Spectrosc Radiat Transfer 1998;59:595–613.
[35] Baranger M. General impact theory of pressure broadening. Phys Rev 1958;112:855–65.
[36] Ben-Reuven A. Spectral line shapes in gases in the binary-collision approximation. In: Prigogine I, Rice SA, editors. Advances in chemical physics. New York: Academic Press; 1975. p. 235.
[37] Hirschfelder JO, Curtiss CF, Bird RB. Molecular theory of gases and liquids. New York: Wiley; 1964.
[38] Sack RA. Two-center expansion for the powers of the distance between two points. J Math Phys 1964;5:260–8.
[39] Neshyba SP, Gamache RR. Improved line broadening coefficients for asymmetric rotor molecules: application to ozone perturbed by nitrogen. J Quant Spectrosc and Radiat Transfer 1993;50:443–53.
[40] Watson JKG. Determination of centrifugal distortion coefficients of asymmetric-top molecules. J Chem Phys 1967;46:1935–49.
[41] Goldman A, Burkholder JB, Howard CJ, Escribano R, Maki AG. Spectroscopic constants for the ν_9 Infrared Band of HNO_3. J Mol Spectrosc 1988;131:195–200.
[42] Maki AG, Wells JS. Measurement and analysis of the fermi resonance between ν_5 and $2\nu_9$ of nitric acid. J Mol Spectrosc 1992;152:69–79.
[43] Huber KP, Herzberg G. Molecular spectra and molecular structure: constants of diatomic molecules. New York: Van Nostrand; 1979.
[44] Cox AP, Riveros JM. Microwave spectrum and structure of nitric acid. J Chem Phys 1965;42:3106–12.
[45] Albinus L, Spieckermann J, Sutter DH. The electric field gradient tensor and the tensors of the molecular magnetic susceptibility and the molecular electric quadrupole moment in nitric acid: a high-resolution rotational Zeeman effect study. J Mol Spectrosc 1989;133:128–47.
[46] Mulder F, van Dijk G, van der Avoird A. Multipole moments, polarizabilities and anisotropic long range interaction coefficients for N_2. Mol Phys 1980;39:407–25.
[47] Bouanich J-P. Site–site Lennard-Jones potential parameters for N_2, O_2, H_2, CO and CO_2. J Quant Spectrosc Radiat Transfer 1992;47:243–50.
[48] Goyette TM, Cohen EA, DeLucia FC. Pressure broadening of HNO_3 by N_2 and O_2: an intercomparison of results in the millimeter wave region. J Quant Spectros Radiat Transfer 1998;60:77–84.
[49] Birnbaum G. Microwave pressure broadening and its application to intermolecular forces. Adv Chem Phys 1967;12:487–548.
[50] Chu WP, Chiou EW, Larsen JC, Thomason LW, Rind D, Buglia JJ, et al. Algorithms and sensitivity analyses for stratospheric aerosol and gas experiment II water vapor retrieval. J Geophys Res 1993;98:4857–66.
[51] Gamache RR, Neshyba SP, Plateaux JJ, Barbe A, Régalia L, Pollack JB. CO_2-broadening of water-vapor lines. J Mol Spectrosc 1995;170:131–51.
[52] Gamache RR, Lynch R, Brown LR. Theoretical calculations of pressure broadening coefficients for H_2O perturbed by hydrogen or helium gas. J Quant Spectros Radiat Transfer 1996;56:471–87.
[53] Wagner G, Birk M, Gamache RR, Hartmann J-M. Collisional parameters of H_2O lines: effects of temperature. J Quant Spectrosc Radiat Transfer 2005;92:211–30.
[54] Toth RA, Brown LR, Smith MAH, Malathy Devi V, Chris Benner D, Dulick M. Air-broadening of H2O as a function of temperature: 696–2163 cm^{-1}. J Quant Spectrosc Radiat Transfer 2006;101:339–66.
[55] Antony BK, Neshyba S, Gamache RR. Self-broadening of water vapor transitions via the complex Robert–Bonamy theory. J Quant Spectrosc Radiat Transfer 2006;105:148–63.
[56] Hartmann JM, Taine J, Bonamy J, Labani B, Robert D. Collisional broadening of rotation–vibration lines for asymmetric-top molecules II. H_2O diode laser measurements in the 400–900 K range calculations in the 300–2000 K range. J Chem Phys 1987;86:144–56.
[57] Gamache RR. Analytical evaluation of the Maxwell–Boltzmann velocity average in pressure-broadened half-width calculations. J Mol Spectrosc 2001;208:79–86.
[58] Zu L, Hamilton PA, Davies PB. Pressure broadening and frequency measurements of nitric acid lines in the 683 GHz region. J Quant Spectros Radiat Transfer 2002;73:545–56.
[59] Goyette TM, Ebenstein WL, Lucia FCD, Helminger P. Pressure broadening of the millimeter and submillimeter wave spectra of nitric acid by oxygen and nitrogen. J Mol Spectrosc 1988;128:108–16.
[60] Goyette TM, Guo W, Delucia FC, Helminger P. Variable temperature pressure broadening of HNO_3 in the millimeter wave spectral region. J Quant Spectrosc Radiat Transfer 1991;46:293–7.
[61] Colmont J-M, Bakri B, Rohart F, Wlodarczak G. Experimental determination of pressure-broadening parameters of millimeter-wave transitions of HNO_3 perturbed by N_2 and O_2, and of their temperature dependences. J Mol Spectrosc 2003;220:52–7.
[62] Cazzoli G, Dore L, Puzzarini C, Bakri B, Colmont J-M, Rohart F, et al. Experimental determination of air-broadening parameters of pure rotational transitions of HNO_3: intercomparison of measurements by using different techniques. J Mol Spectrosc 2005;229:158–69.